

Th A12 08

3-D Time-Domain VTI Viscoacoustic Full Waveform Inversion: Application to Valhall Field Data

P. Yang* (Univ. Grenoble Alpes, ISTerre), R. Brossier (Univ. Grenoble Alpes, ISTerre), L. Metivier (Univ. Grenoble Alpes - CNRS, LJK), J. Virieux (Univ. Grenoble Alpes, ISTerre)

Summary

This work presents a first 3D field data application to the OBC Valhall dataset of a recently developed vertical transverse isotropic (VTI) viscoacoustic full waveform inversion (FWI) engine, incorporating attenuation as a passive parameter. Our implementation uses a checkpointing-assisted reverse-forward simulation (CARFS) algorithm to efficiently build the FWI gradient, appearing more efficient than standard checkpointing techniques. The reverse propagation of the incident field is performed stably in attenuating medium with low memory cost, thanks to the decimation and interpolation strategy. We follow a frequency-content continuation workflow: starting from low frequencies, each FWI takes the refined velocity model and re-estimates a new source wavelet at given frequency band, combined with a random shots subsampling. The inverted velocity model clearly captures channel features and gas cloud, in agreement with former studies (Sirgue 2010, Operto 2015). Estimated source wavelets using this final inverted model show good consistency over shots. The synthetic data can match the observed seismograms quite well with an anisotropic visco-acoustic forward problem engine. This encouraging single-parameter inversion for a real case motivates multiparameter inversion in the time domain while keeping cross-talk effects small.

Introduction

Full waveform inversion (FWI) is a powerful technique to build high resolution subsurface mechanical properties estimations. Current challenges for applications of this strategy involve the imaging of large scale complex targets, for which an accurate description of the wave propagation is required, accounting in particular for attenuation and anisotropy. Frequency-domain approaches easily account for the attenuation through complex wave velocities and recently Operto et al. (2015) has shown how it improves the model reconstruction. However, current implementations of frequency approaches are still limited by heavy memory consumption using direct solvers. Previous approaches in time-domain anisotropic acoustic formulation were not considering attenuation effects (Warner et al., 2013). Is the introduction of attenuation either in the forward and/or in the inverse problems feasible for 3D targets in time domain? This is the objective of this presentation.

However, efficient time-domain FWI algorithms present different difficulties due to the time description of the complex wave physics related to attenuation. Based on generalized Maxwell body (GMB) with a few relaxation mechanisms, we can approximate a constant quality factor over the seismic frequency band. The gradient is built using the checkpointing-assisted reverse-forward simulation (CARFS) algorithm (Yang et al., 2016b) to maximize the computational efficiency while maintaining a low memory cost, coupled with a decimation/interpolation strategy for reconstructing the incident field using its values stored at the boundaries (Yang et al., 2016c). We apply these tools to 3D field dataset studied in frequency-domain by Operto et al. (2015), to reconstruct the P-wave velocity, using attenuation as a passive parameter.

Method: Time-domain VTI viscoacoustic FWI

The objective of the FWI is to minimize the misfit between the observed seismograms \mathbf{d}_{obs} and the synthetic data \mathbf{d}_{cal} . In least-squares sense, the misfit function is $\chi(\mathbf{m}) = \frac{1}{2} \|\mathbf{d}_{cal}(\mathbf{m}) - \mathbf{d}_{obs}\|^2$, where \mathbf{m} is a vector including all the model parameters. The synthetic data \mathbf{d}_{cal} has to be extracted from the incident wavefield \mathbf{w} at the receiver locations via the restriction operator $\mathbf{d}_{cal}(\mathbf{m}) = R_r \mathbf{w}$. Assuming isotropic attenuation using GMB under VTI visco-acoustic approximation, the forward and the adjoint wave equations including particle velocity \mathbf{v} , stress $\boldsymbol{\sigma}$ and the memory variables ξ_ℓ and their adjoint variables $\bar{\mathbf{v}}$, $\bar{\boldsymbol{\sigma}}$ and $\bar{\xi}_\ell$ reads

$$\underbrace{\begin{bmatrix} \rho \partial_t & D^\dagger & \dots & 0 & \dots \\ -D & C^{-1} \partial_t & \dots & Y_\ell & \dots \\ \vdots & \vdots & \ddots & \vdots & \vdots \\ -D & 0 & \dots & \frac{1}{\omega_\ell} \partial_t + I & \dots \\ \vdots & \vdots & \vdots & \vdots & \ddots \end{bmatrix}}_{A(\mathbf{m})} \underbrace{\begin{bmatrix} \mathbf{v} \\ \boldsymbol{\sigma} \\ \vdots \\ \xi_\ell \\ \vdots \end{bmatrix}}_{\mathbf{w}} = \underbrace{\begin{bmatrix} \mathbf{f}_v \\ C^{-1} \mathbf{f}_\sigma \\ \vdots \\ 0 \\ \vdots \end{bmatrix}}_{\mathbf{s}}, \quad \underbrace{\begin{bmatrix} -\rho \partial_t & -D^\dagger & \dots & -D^\dagger & \dots \\ -D & -C^{-1} \partial_t & \dots & 0 & \dots \\ \vdots & \vdots & \ddots & \vdots & \vdots \\ 0 & Y_\ell & \dots & -\frac{1}{\omega_\ell} \partial_t + I & \dots \\ \vdots & \vdots & \vdots & \vdots & \ddots \end{bmatrix}}_{A^\dagger(\mathbf{m})} \underbrace{\begin{bmatrix} \bar{\mathbf{v}} \\ \bar{\boldsymbol{\sigma}} \\ \vdots \\ \bar{\xi}_\ell \\ \vdots \end{bmatrix}}_{\bar{\mathbf{w}}} = \underbrace{\begin{bmatrix} \Delta d_v \\ \Delta d_\sigma \\ 0 \\ \vdots \\ 0 \end{bmatrix}}_{R^\dagger \Delta \mathbf{d}}, \quad (1)$$

where D is a spatial differential operator; \mathbf{m} gathers the density ρ , the elastic stiffness tensor C (parameterized by P-wave velocity V_p and Thomsen parameters ε and δ under vertical transverse isotropic (VTI) approximation (Yang et al., 2018)), and the attenuation factor Q^{-1} embedded in the anelastic coefficients $Y_\ell \approx y_\ell Q^{-1}$; \mathbf{w} , $\bar{\mathbf{w}}$ and $R^\dagger \Delta \mathbf{d}$ are the incident field, the adjoint field and the backward projected data residuals. Away from the source location, the gradient of the misfit function is thus given by $\nabla_{\mathbf{m}} \chi = \int_0^T dt \bar{\mathbf{w}}^\dagger \frac{\partial A(\mathbf{m})}{\partial \mathbf{m}} \mathbf{w}$, which is a zero-lag cross-correlation between the forward field \mathbf{w} and the adjoint field $\bar{\mathbf{w}}$ weighted by the scattering matrix $\partial A(\mathbf{m}) / \partial \mathbf{m}$ (Yang et al., 2016a). At each iteration, the model is updated $\mathbf{m}^{k+1} = \mathbf{m}^k + \alpha \Delta \mathbf{m}^k$ following a descent direction $\Delta \mathbf{m}^k = -H(\mathbf{m}^k)^{-1} \nabla_{\mathbf{m}} \chi(\mathbf{m}^k)$ where α is the step length estimated via line search, while the Hessian inverse $H(\mathbf{m}^k)^{-1}$ is approximated using the L-BFGS algorithm (Nocedal and Wright, 2006).

Our implementation relies on SEISCOPE optimization toolbox (Métivier and Brossier, 2016). To avoid a huge memory consumption, we first simulate the incident wavefield while saving its values only on at the boundaries at Nyquist time step. We then backpropagate the incident and adjoint wavefields simultaneously, while the missing values at the boundary are interpolated at each time step (Yang et al., 2016c). Due to the existence of seismic attenuation, we resort to our checkpointing-assisted reverse-forward simulation (CARFS) algorithm to backpropagate the incident wavefield: Using an energy measure to detect the instability of reverse propagated incident field, CARFS gains much better efficiency compared to the conventional optimal checkpointing algorithm (Yang et al., 2016b).

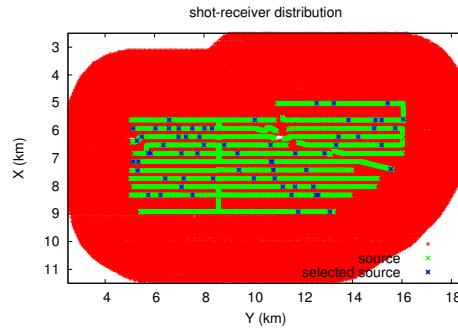


Figure 1 Layout of the 3D Valhall OBC dataset: Shots and receivers are switched for inversion efficiency based on reciprocity.

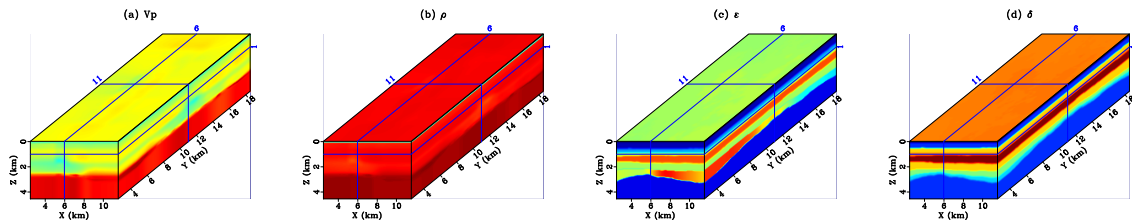


Figure 2 Initial model: (a) V_p ; (b) ρ ; (c) ϵ , (d) δ and $Q=200$

3-D inversion for Valhall field data

The Valhall oil field is located in the North Sea in a shallow water environment (70 m of water depth). The low velocity zone associated with the gas cloud creates a significant attenuation footprint, making seismic imaging at the reservoir depths challenging (Sirgue et al., 2010; Prioux et al., 2011, 2013a; Operto et al., 2015). Twelve ocean bottom cables (OBCs) involving 2302 four-component receivers record 49 954 shots, located 5 m below the sea surface, and cover a surface of 145 km² (Operto et al., 2015). Fig. 1 displays the layout of the permanent 3D OBC acquisition, where the sources and receivers have been switched to reduce the computational cost in the inversion according to the reciprocity. The inline spacing between two consecutive shots and receivers is 50 m.

Anisotropic modeling has been shown to be essential to invert for Valhall field data (Prioux et al., 2011), to guarantee the correct estimation of the P-wave kinematics. In this study, we focus on mono-parameter V_p inversion (starting from the tomographic velocity model as shown Fig. 2a), while other parameters are fixed (density, Thomsen's parameters ϵ and δ , see Fig. 2b-d). The density model is deduced using Gardner's law. To fit the early arrivals at long offset, incorporating attenuation in the simulation of the wave propagation proves to be essential to account for the strong attenuation effects in the gas cloud (Prioux et al., 2011, 2013b). A constant attenuation model ($Q=200$) is used, as done in Operto et al. (2015). Three GMB mechanisms ($L = 3$) simulate absorption and dispersion effects of the nearly constant Q propagation. The VTI viscoacoustic wave equation and its adjoint are discretized using leap-frog staggered grid finite difference scheme, with free surface boundary condition on the top, and sponge absorbing boundary condition elsewhere. Ten checkpoints following the binomial law store wavefield snapshots for CARFS algorithm. Since CARFS also needs stored boundaries for reverse propagation of the incident field requested by the FWI gradient computation, the boundary storage sampling are decimated with a factor of 10 with respect to the CFL time-step. Finally, l-BFGS algorithm combined with depth preconditioning to compensate for geometrical spreading is used.

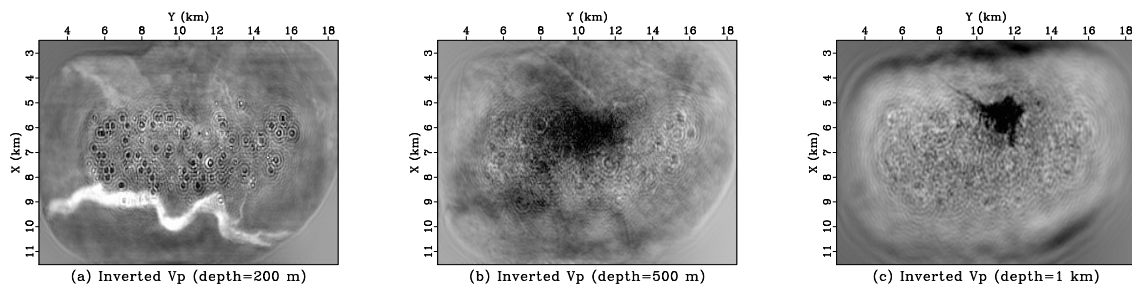


Figure 3 Inverted velocity at depth (a) 200 m, (b) 500 m and (c) 1 km. Note that the imprint of the randomly selected shots appears in the shallow (200 m) depth slice.

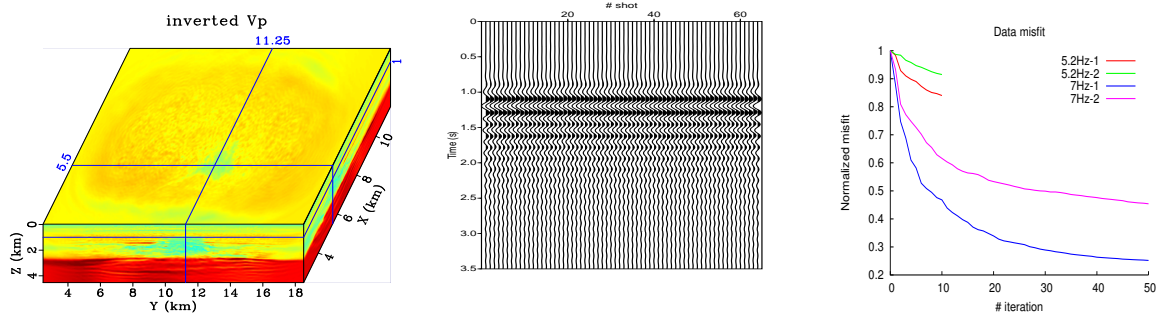


Figure 4 (a) 3-D view of final inverted velocity; (b) Estimated source wavelet for each shot as a quality control; (c) Data misfit during the inversion at different frequency bands.

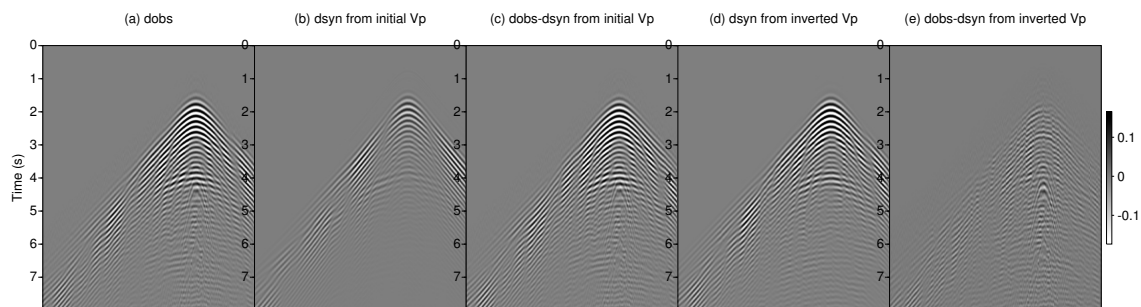


Figure 5 Comparison of the data match (extracted from one line of one shot): (a) observed data after bandpass filtering at frequency 2.5–7 Hz; (b) synthetic data using initial Vp; (c) data residual using initial model; (d) synthetic data using inverted Vp; (e) data residual using inverted Vp (the shear waves are not expected to be matched due to acoustic approximation).

The inversion is conducted in a multiscale manner, to mitigate potential cycle skipping issues (Bunks et al., 1995). The observed seismic data is first filtered into two frequency bands: 2.5–5.2 Hz and 2.5–7 Hz. For each frequency band, we perform two inversions using a subset of randomly chosen 64 shots among the 2302 available shots, as indicated in Fig. 1. Each inversion takes the inverted model in the previous stage as an initial guess, deduces a new density model according to Gardner’s law and estimates a source wavelet (Pratt, 1999) in a pre-processing step. The first inversion for 2.5–5.2 Hz starts with the initial models shown in Fig. 2 (resampled with 70 m grid spacing, leading to smaller numbers of gridpoints). For the low frequency part, we only perform 10 iterations as we do not expect a high resolution imaging at the very beginning. A Gaussian smoothing is also applied to the gradient. The correlation length in a given direction is a fraction of the local wavelength, which is decreased for the second stage of the inversion in this frequency band.

We resample the inverted model at 2.5–5.2 Hz to 50 m grid spacing to start our 1st inversion at 2.5–7 Hz, with slight gradient smoothing. The second inversion at 2.5–7 Hz does not use any smoothing, resulting in a high resolution velocity model showing different features already noticed (Sirgue et al., 2010; Operto et al., 2015): from the inverted velocity at 200 m depth (Fig. 3), we clearly see the shallow channels; besides, the footprint of shot location in the FWI inverted model are visible. The depth slice at 500 m shows the imprint of the drift of glacier, as interpreted by (Sirgue et al., 2010). At 1 km depth, we are able to catch the top of the low velocity anomaly with detailed contour. Fig. 4a gives a 3D view of the inverted velocity model. As a further quality control, in Fig. 4b we show the estimated source wavelets from each shot in the final velocity model: the consistency of the estimated sources is very good. In Fig. 4c, we plot the evolution of the misfit function at all the inversion steps, which indicates a satisfactory decrease of the data misfit, in particular at higher frequencies for which the signal to noise ratio is better. The synthetic data simulated from the initial velocity model (Fig. 5b) cannot match the observed data (Fig. 5a), leading to big differences (Fig. 5c). After the 3-D viscoacoustic inversion, the simulated data (Fig. 5d) matches the observations quite well, resulting in reasonably small data residuals (Fig. 5e), because the expression of shear waves is quite small in these records.

Conclusion and perspectives

We have successfully applied 3D time-domain visco-acoustic FWI to the OBC Valhall field data. Three ingredients are essential for this application: the use of GMB to obtain a realistic attenuation with an

almost constant quality factor in the frequency band we consider, the use of a decimation and interpolation strategy, and the CARFS algorithm to reduce the memory consumption with improved efficiency to building the FWI gradient in attenuating medium. The inverted velocity model is consistent with the former studies (Sirgue et al., 2010; Operto et al., 2015). Up to now, our study focuses on mono-parameter inversion for V_p , while other parameters are fixed during the iterations. The obtained high resolution velocity model provides a good starting point to study further multiparameter FWI. The truncated Newton algorithm and a multi-parameter preconditioner are tools designed to reduce potential inter-parameter cross-talks and obtain more reliable second-order parameters such as density or attenuation (Yang et al., 2018). We seek to exploit these methods on this 3D real field dataset for assessing feasibility and interest of extracting multiple parameters with mitigation of cross-talks.

Acknowledgements

This study was partially funded by the SEISCOPE consortium (<http://seiscope2.osug.fr>), sponsored by AKERBP, CGG, CHEVRON, EXXON-MOBIL, JGI, PETROBRAS, SCHLUMBERGER, SHELL, SINOPEC, STATOIL and TOTAL. This study was granted access to the HPC resources of SIGAMM infrastructure (<http://crimson.oca.eu>) and CINES/IDRIS/TGCC under the allocation 046091 made by GENCI. We appreciate AKERBP ASA and HESS AS for providing the data set and the permission to publish this work, the help from Stéphane Operto to understand the data, and constructive comments of Ross Milne from AKERBP.

References

- Bunks, C., Salek, F.M., Zaleski, S. and Chavent, G. [1995] Multiscale seismic waveform inversion. *Geophysics*, **60**(5), 1457–1473.
- Métivier, L. and Brossier, R. [2016] The SEISCOPE optimization toolbox: A large-scale nonlinear optimization library based on reverse communication. *Geophysics*, **81**(2), F11–F25.
- Nocedal, J. and Wright, S.J. [2006] *Numerical Optimization*. Springer, 2nd edn.
- Operto, S., Miniussi, A., Brossier, R., Combe, L., Métivier, L., Monteiller, V., Ribodetti, A. and Virieux, J. [2015] Efficient 3-D frequency-domain mono-parameter full-waveform inversion of ocean-bottom cable data: application to Valhall in the visco-acoustic vertical transverse isotropic approximation. *Geophysical Journal International*, **202**(2), 1362–1391.
- Pratt, R.G. [1999] Seismic waveform inversion in the frequency domain, part I: theory and verification in a physical scale model. *Geophysics*, **64**, 888–901.
- Prieux, V., Brossier, R., Gholami, Y., Operto, S., Virieux, J., Barkved, O. and Kommedal, J. [2011] On the footprint of anisotropy on isotropic full waveform inversion: the Valhall case study. *Geophysical Journal International*, **187**, 1495–1515.
- Prieux, V., Brossier, R., Operto, S. and Virieux, J. [2013a] Multiparameter full waveform inversion of multicomponent OBC data from Valhall. Part 1: imaging compressional wavespeed, density and attenuation. *Geophysical Journal International*, **194**(3), 1640–1664.
- Prieux, V., Lambaré, G., Operto, S. and Virieux, J. [2013b] Building starting model for full waveform inversion from wide-aperture data by stereotomography. *Geophysical Prospecting*, **61**(Issue supplement: 60 year anniversary issue), 109–137.
- Sirgue, L., Barkved, O.I., Dellinger, J., Etgen, J., Albertin, U. and Kommedal, J.H. [2010] Full waveform inversion: the next leap forward in imaging at Valhall. *First Break*, **28**, 65–70.
- Warner, M., Ratcliffe, A., Nangoo, T., Morgan, J., Umpleby, A., Shah, N., Vinje, V., Stekl, I., Guasch, L., Win, C., Conroy, G. and Bertrand, A. [2013] Anisotropic 3D full-waveform inversion. *Geophysics*, **78**(2), R59–R80.
- Yang, P., Brossier, R., Métivier, L. and Virieux, J. [2016a] A review on the systematic formulation of 3D multiparameter full waveform inversion in viscoelastic medium. *Geophysical Journal International*, **207**(1), 129–149.
- Yang, P., Brossier, R., Métivier, L. and Virieux, J. [2016b] Wavefield reconstruction in attenuating media: A Checkpointing-assisted reverse-forward simulation method. *Geophysics*, **81**(6), R349–R362.
- Yang, P., Brossier, R., Métivier, L., Virieux, J. and Zhou, W. [2018] A time-domain preconditioned truncated Newton approach to multiparameter visco-acoustic full waveform inversion. *SIAM Journal on Scientific Computing*, submitted.
- Yang, P., Brossier, R. and Virieux, J. [2016c] Wavefield reconstruction from significantly decimated boundaries. *Geophysics*, **80**(5), T197–T209.